Molecular Basis for Substrate Selectivity and Specificity by an LPS Biosynthetic Enzyme[†,‡]

Yaozhong Zou,[§] Chong Li,[§] Joseph S. Brunzelle,[⊥] and Satish K. Nair*[,§,||]

Department of Biochemistry and Center for Biophysics and Computational Biology, University of Illinois at Urbana-Champaign, 600 S. Mathews Avenue, Urbana, Illinois 61801, and Life Sciences Collaborative Access Team, Argonne National Laboratory, Argonne, Illinois 60439

Received May 26, 2006; Revised Manuscript Received December 1, 2006

ABSTRACT: Diversity in the polysaccharide component of lipopolysaccharide (LPS) contributes to the persistence and pathogenesis of Gram-negative bacteria. The Nudix hydrolase GDP-mannose mannosyl hydrolase (Gmm) contributes to this diversity by regulating the concentration of mannose in LPS biosynthetic pathways. Here, we present seven high-resolution crystal structures of Gmm from the enteropathogenic *E. coli* strain O128: the structure of the apo enzyme, the cocrystal structure of Gmm bound to the product Mg^{2+}−GDP, two cocrystal structures of precatalytic and turnover complexes of Gmm-Ca^{2+}−GDP-α-D-mannose, and three cocrystal structures of an inactive mutant (His-124 → Leu) Gmm bound to substrates GDP-α-D-mannose, GDP-α-D-glucose, and GDP-β-L-fucose. These crystal structures help explain the molecular basis for substrate specificity and promiscuity and provide a structural framework for reconciling previously determined kinetic parameters. Unexpectedly, these structures reveal concerted changes in the enzyme structure that result in the formation of a catalytically competent active site only in the presence of the substrate/product. These structural views of the enzyme may provide a rationale for the design of inhibitors that target the biosynthesis of LPS by pathogenic bacteria.

Lipopolysaccharide (LPS) is the major constituent of the outer membrane of Gram-negative bacteria. LPS is composed of a lipid core (lipid A) attached to a variant polysaccharide group. The lipid A region mediates the toxicity of LPS (*1*), whereas the variable polysaccharide contributes to the heterogeneity of LPS (*2*). Variations of the polysaccharide component of bacterial LPS are found in the polysaccharide side chains termed the bacterial *O*-antigen (*3*). The composition of the *O*-antigen varies among different Gram-negative bacterial strains, and this diversity is dictated by the nature, order, and linkage of the different sugars within the polysaccharide (*4*). Diversity of the polysaccharide side chains allows the pathogen to evade the host's immune response and subsequent phagocytotic engulfment.

The *O*-antigen consists of at least 20 different sugars, and this diversity is important for its biological function (*5*). The genes involved in the biosynthesis of the *O*-antigen are usually found as a gene cluster and are transcribed as a unit (*6*). These gene products fall into three major classes: proteins involved in the biosynthesis of the nucleotide sugar precursors, glycosyltransferases that attach the precursor sugars onto a lipid molecule on the cytoplasmic side of the inner membrane, and processing proteins that mediate membrane translocation and polymerization (*7*).

The *O*-antigen clusters of several pathogenic *E. coli* and *S. enterica* strains encode another member of the first major class, GDP-α-D-mannose mannosyl hydrolase (Gmm[1]) (*8*). Gmm catalyzes the hydrolysis of GDP-α-D-mannose into GDP and mannose (*9*) (Figure 1). By preventing the accumulation of high concentrations of GDP-α-D-mannose in the sugar biosynthetic pathway, Gmm can regulate the amount of mannose and maintain sugar diversity in the *O*-antigen (*9*).

Sequence comparisons and mutational studies place Gmm within the Nudix hydrolase superfamily of enzymes (*9*, *10*). Nudix enzymes are typically pyrophosphatases that catalyze the hydrolysis of nucleotide diphosphates and their derivatives. These enzymes exhibit a common structural fold, termed the Nudix fold, punctuated by the presence of the Nudix signature sequence $GX_5EX_7REUXEEGU$ (where *U* = leucine, isoleucine, or valine, and *X* = any residue) (*11*). Gmm falls within a subclass of Nudix enzymes that cleave the phosphoglycosyl bond between nucleotide sugars by nucleophilic substitution at carbon-1 (*10*). Thus, the Gmm family of Nudix enzymes are sugar nucleotide hydrolases rather than pyrophosphatases.

The crystal structure of the Gmm-Mg^{2+}−GDP product complex, from the nonpathogenic *E. coli* K12 strain, reveals

[†] This work is supported in part by a grant from the American Cancer Society and startup funds from the University of Illinois.

[‡] The following pdb codes were deposited in the Protein Data Bank: 218O, 218P, 218Q, 218R, 218S, 218T, and 218U.

* To whom correspondence should be addressed. Tel: (217) 333-2688. Fax: (217) 244-5858. E-mail: snair@uiuc.edu.

[§] Department of Biochemistry, University of Illinois at Urbana-Champaign.

[||] Center for Biophysics and Computational Biology, University of Illinois at Urbana-Champaign.

[⊥] Argonne National Laboratory.

[1] Abbreviations: GDP, guanosine 5′-(trihydrogen diphosphate); Gmm, GDP-mannose mannosyl hydrolase; HEPES, 4-(2-hydroxyethyl)-1-piperazineethanesulfonic acid.

10.1021/bi061056u CCC: $37.00
Published on Web 03/20/2007

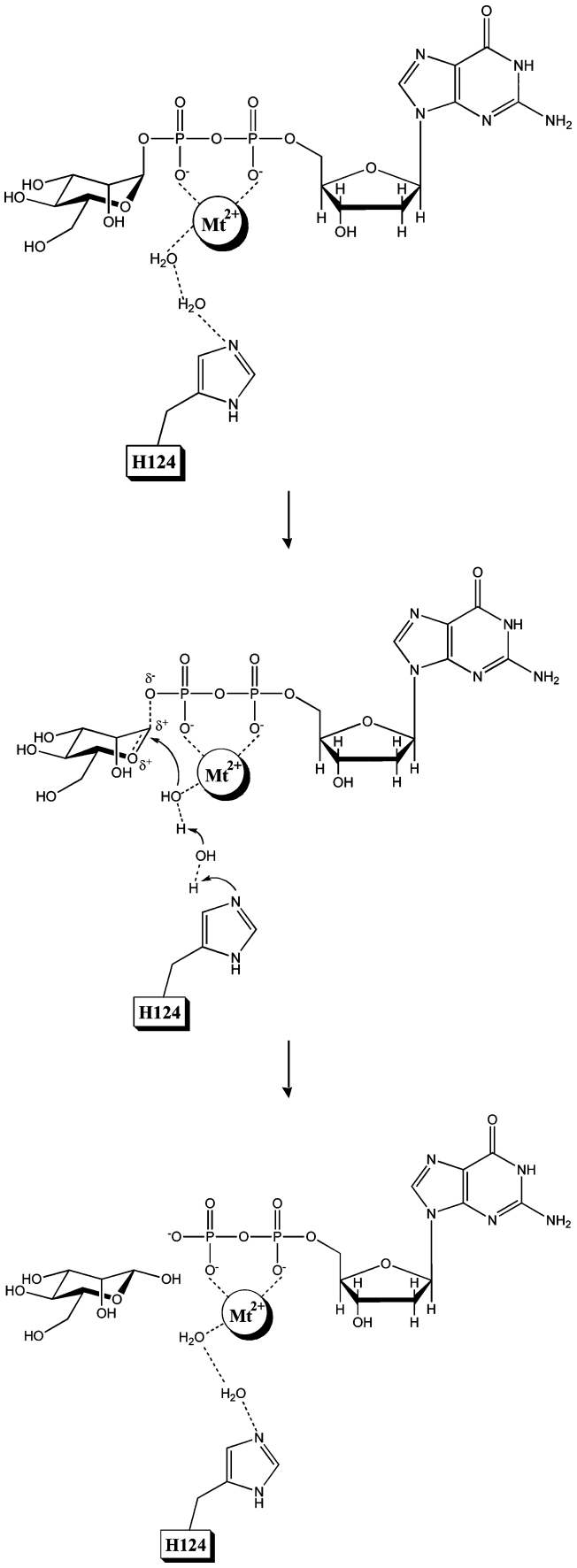

FIGURE 1: Schematic representation of the mechanism of action proposed for the hydrolysis of GDP-α-D-mannose as catalyzed by Gmm. The proposed oxocarbenium character of the transition state is consistent with prior studies (*25*). The identity of the residues shown to be involved in interactions with the substrate and product is based on biochemical data (*11*).

a canonical Nudix fold augmented with an amino terminal loop−helix extension (*12*). The GDP product is shown to bind to an internal cavity created by the α-helical segment of this extension. Finally, the switch in specificity from a pyrophosphatase to sugar nucleotide hydrolase is explained by a shortening of the loop containing the putative catalytic base such that substitution occurs at C1 of the sugar (*12*).

Here, we describe seven high-resolution crystal structures of Gmm from the O128 antigenic subgroup of enteropathogenic *E. coli*. We have determined the structure of the unliganded *E. coli* O128 Gmm, the cocrystal structure with product GDP, and three cocrystal structures of an inactive mutant (His-124 → Leu) bound to GDP-α-D-mannose, GDP-α-D-glucose, and GDP-*β*-L-fucose. In addition, we have also determined two high-resolution crystal structures of wild-type Gmm bound to the substrate GDP-α-D-mannose. For the first of these structures, we used crystals, harvested immediately after growth, of Gmm−GDP-α-D-mannose in which the catalytically requisite divalent magnesium ion was replaced with calcium in order to determine the structure of an unreacted ternary complex. Our kinetic studies demonstrate that substitution of calcium compromises the catalytic efficiency of the enzyme, thus facilitating structural analysis of the precatalytic ternary complex. The second crystal structure of Gmm-Ca^{2+}−GDP-α-D-mannose, from crystals that had incubated in the crystallization media for an addtional 72 h, reveals a product complex and demonstrates that the enzyme is active in the crystal. These crystal structures (*1*) reveal the determinants of substrate and product binding by the enzyme, (*2*) explain the molecular basis for substrate promiscuity, and (*3*) provide a structural rationale for understanding the kinetic parameters previously established for each of these different substrates. Progress along the reaction coordinate of GDP-α-D-mannose hydrolysis is characterized by a significant conformational change at the active site. These crystal structures detail concerted changes in the enzyme structure that track the formation of a competent active site during progress along the catalytic reaction coordinate.

MATERIALS AND METHODS

Enzyme Cloning, Expression, and Purification. Escherichia coli antigenic subgroup O128 (*13*) was purchased from the American Tissue Culture Collection, and genomic DNA was extracted using standard molecular biological methodology (*14*). The gene encoding the Gmm−GDP-α-D-mannose mannosyl hydrolase was cloned by the polymerase chain reaction using primers designed on the basis of the published sequence (*15*). The sequence of the forward primer is 5′-aagcagccgCATATGatgtttttacgtcaggaagactttgcc-3′ with an engineered Nde I restriction site (shown in capital letters) preceding the start codon. The sequence of the reverse primer is 5′-ccgCTCGAGtcagacatttttgacttccttttttatttaagcc-3′ with an engineered Xho I restriction site (shown in capital letters) following an engineered stop codon. The gene was inserted into a pET-14 plasmid (Novagen) bearing an amino terminal polyhistidine tag and a thrombin digestion site preceding the inserted gene. The Quickchange (Stratagene) system was used to generate the His-124 → Leu variant. The integrity of all constructs and their variants were confirmed by sequencing.

E. coli expression strain BL21(DE3) was transformed with the appropriate expression vectors, and single colonies of transformed *E. coli* were used to inoculate 5 mL of LB medium supplemented with ampicilin (100 μg/mL). Five hours following inoculation, the small-scale culture was added to 1 L of LB medium containing ampicilin (100 μg/mL) for growth at 37 °C. When the A_{600nm} value of the culture reached 0.5, protein expression was induced with 0.5 mM isopropyl-β-D-thiogalactopyranoside, and the cells were further grown overnight at 18 °C. Bacterial cells were pelleted by centrifugation (4000*g* for 1 h) and resuspended in 100 mM KCl, 20 mM Tris-HCl (pH 8.3), 10% glycerol, and a cocktail of protease inhibitors. Resuspended cells were disrupted by multiple passes through an Avestin C5 Emulsiflex French press cell, and insoluble aggregates and cellular debris were removed by centrifugation (15 000*g* for 1 h).

Recombinant Gmm was purified from the clarified supernatant by virtue of the amino terminal polyhistidine tag using a Talon resin (Clontech) column charged with cobalt chloride. Following elution from the cobalt affinity resin, the cleavable polyhistidine tag was removed using thrombin (1 U/mg protein, G.E. Healthcare). The protein was further purified by anion exchange (5 mL HiTrap Q, G. E. Healthcare) and size exclusion chromatography (Superdex 75 16/60, G. E. Healthcare) prior to crystallization. Site-specific variants were purified in essentially the same manner. Selenomethionine incorporated Gmm was produced by the method of van Duyne et al. (*16*) and purified in the manner described above except that 5 mM β-mercaptoethanol was added to all of the buffers. The protein samples were estimated to be greater than 95% pure as judged by SDS−polyacrylamide gel electrophoresis.

Substrate and Product. GDP, GDP-α-D-mannose, GDP-α-D-glucose, and GDP-β-L-fucose were purchased from Sigma and used without further purification.

Enzyme Assay. Steady-state kinetic experiments to measure the hydrolysis of GDP-α-D-mannose by Mg^{2+}- or Ca^{2+}-activated Gmm were performed as described (*10*, *12*). Briefly, the assay measures the amount of GDP produced by the hydrolysis of GDP-α-D-mannose by measuring the concentration of phosphate produced by the treatment of the product with calf intestinal alkaline phosphatase in a coupled enzyme assay. The GDP-α-D-mannose substrate is not cleaved by alkaline phosphatase. These assays were performed with saturating concentrations of either Mg^{2+} or Ca^{2+} such that the reaction was regarded as a single substrate reaction. Each 50 μL reaction contained 80 mM HEPES at pH 7.5, 20 mM of the either Mg^{2+} or Ca^{2+}, and 0.05 μg of enzyme. The following concentrations of GDP-α-D-mannose were used: 0.2, 0.5, 1, 2, and 5 mM. The reaction was allowed to proceed at 20 °C for 20 min, and terminated by heat treatment at 95 °C for 3 min. The reactions were then treated with alkaline phosphatase (1 unit) at 37 °C for 11 min in order to release the phosphate group from GDP. A 250 μL volume of 5 mM EDTA and 700 μL of Ames mix (1 part of 10% ascorbic acid and 6 parts of 0.42% ammonium molybdate in 1 N H_2SO_4) were added to the reaction mixtures, and the reactions were incubated at 37 °C for 30 min. The concentration of molybdate phosphate was determined by measuring the absorbance at 780 nm using potassium phosphate as the standard. Each experiment was replicated in triplicate in order to minimize errors (Table 1).

Table 1: Kinetic Parameters for Metal-Substituted Gmm

	GDP-α-D-mannose		
	k_{cat} (s^{-1})	K_M (mM)	k_{cat}/K_M (s^{-1} mM^{-1})
magnesium	0.16 ± 0.02	0.75 ± 0.18	0.21
calcium	0.054 ± 0.012	2.36 ± 0.47	0.023

Crystallization. Initial crystallization conditions were established by sparse-matrix sampling methods using commercial (Crystal Screens I, II and Natrix from Hampton Research; Wizard Screens I, II, and III from Emerald Biosystems) and homemade screens. Refinement of promising conditions yielded large crystals suitable for diffraction analysis. Crystals of *E. coli* O128 Gmm were grown using the hanging drop vapor diffusion method. Briefly, 2 μL of the protein sample (10 mg/mL) was added to 2 μL of the precipitant (10−20% polyethylene glycol 4000, 200 mM sodium acetate, 100 mM HEPES at pH 8.0, and 10 mM of $MgSO_4$) and equilibrated over a well containing the precipitant solution at 20 °C. Crystals grew in 24 h and reached a maximum size of 0.3 × 0.3 × 0.6 mm^3 in 3 days. Cocrystals of the wild-type Gmm-Mg^{2+}−GDP and Gmm-Ca^{2+}−GDP-α-D-mannose complexes and His-124 → Leu Gmm−ligand complexes were grown under similar conditions (with 10 mM of either $MgSO_4$ or $CaSO_4$ and 10 mM of the appropriate ligand), but the equilibration temperature was 8 °C. In order to obtain cocrystals of the wild-type enzyme−substrate complex, crystals of Gmm-Ca^{2+}−GDP-α-D-mannose were harvested and cryo-cooled immediately after growth (approximately 12 h following the initiation of crystallization). In order to demonstrate turnover in the crystal, we utilized cocrystals of Gmm-Ca^{2+}−GDP-α-D-mannose that were incubated in the crystallization drop for an additional 72 h at 8 °C and were then harvested and cryo-cooled. Because the crystallization precipitant proved to be suitable for cryoprotection, single crystals were harvested straight from the crystallization drop and flash cooled in liquid nitrogen prior to data collection.

X-ray Data Collection and Structure Determination. Flash-cooled crystals of unliganded, Se-Met labeled Gmm diffracted X-rays to a minimum Bragg spacing of 1.8 Å using an insertion device X-ray beam line utilizing a ADSC Q4 CCD detector (BIOCARS-Sector 14ID, Advanced Photon Source, Argonne, IL). A 4-fold redundant data set was collected from crystals flash cooled to 100 K in a single 180° sweep at the selenium edge (Table 2). These crystals occupied space group $P2_12_12_1$ with unit cell parameters a = 49.4 Å, b = 79.6 Å, and c = 94.5 Å. The structure was solved by single-wavelength anomalous diffraction utilizing anomalous scattering from the two selenium-substituted methionines per monomer of Gmm. Data were indexed and scaled using the HKL2000 package (*17*). Four selenium sites, corresponding to the two molecules of Gmm in the asymmetric unit, were identified and further refined using SOLVE (*18*), yielding an initial figure of merit of 0.39−2.2 Å resolution (Table 1). Solvent flattening with RESOLVE further improved the quality of the initial map and permitted almost 85% of main chain and 29% of side chain residues to be automatically built by the software (*19*). The remainder of the model was fitted using XtalView (*20*) and further improved by rounds of refinement with REFMAC5 (*21*) and

Table 2: Data Collection and Refinement Statistics

Data collection Statistics

	apo-Gmm	Gmm-GDP	GDP-α-D-Man	GDP-α-D-Gluc	GDP-β-L-Fuc	precatalytic	turnover
space group	$P2_12_12_1$	$P2_12_12_1$	$P2_12_12_1$	$P2_12_12_1$	$P2_12_12_1$	$P2_12_12_1$	$P2_12_12_1$
cell dimensions (Å)	$a = 49.4$	$a = 49.5$	$a = 48.9$	$a = 49.1$	$a = 48.9$	$a = 49.6$	$a = 49.6$
	$b = 79.6$	$b = 80.7$	$b = 77.5$	$b = 75.4$	$b = 70.6$	$b = 81.6$	$b = 81.2$
	$c = 94.5$	$c = 98.0$	$c = 92.7$	$c = 92.3$	$c = 89.3$	$c = 98.3$	$c = 97.9$
resolution (Å)	1.9 (1.97)	1.5 (1.55)	2.0 (2.07)	2.1 (2.16)	2.0 (2.07)	1.3 (1.35)	1.4 (1.45)
total observations	201,773	237,730	137,299	73,886	105,268	360,764	374,501
unique reflections	29,041	63,778	24,313	20,452	21,132	94,585	77,746
completeness (%)	99.5 (99.5)	98.9 (99.1)	99.4 (100)	98.6 (96.9)	95.7 (92.1)	95.8 (81.2)	98.7 (96.4)
R_{merge} (%)[c]	3.9 (8.7)[a]	3.7 (16.9)[a]	5.7 (15.8)[a]	5.2 (26.3)	5.6 (16.9)[a]	4.0 (14.9)[a]	4.0 (14.9)
$I/\sigma(I)$	59 (23)[a]	57 (13)[a]	27 (10)[a]	24 (4)[a]	21 (8)[a]	29 (5)[a]	29 (5)

SAD Analysis

wavelength (Å)	0.9686
phasing resolution	2.2 Å
mean FOM	0.39
density modified FOM	0.73

Refinement Statistics

	Apo-Gmm	Gmm-GDP	GDP-α-D-Man	GDP-α-D-Gluc	GDP-β-L-Fuc	precatalytic	turnover
resolution range (Å)	24.7−1.9	23.7−1.5	43−2.0	23−2.1	37−2.0	42−1.3	29−1.4
reflections used	26,869	59.027	22,655	26,651	19,561	87,720	72,076
$R_{crystal}/R_{free}$ (%)[d]	19.4/24.4	17.8/19.0	20.2/25.1	20.6/24.4	21.1/24.8	14.9/17.1	13.9/16.5
number of atoms							
protein	2618	2433	2505	2436	2277	2448	2448
ligand	n/a	56	39[b]	39[b]	39[b]	78	56
solvent	354	332	140	146	70	593	557
average B value (Å^2)	20.9	13.8	42.3	46.8	34.9	8.5	8.7
rmsd length (Å)	0.013	0.010	0.016	0.018	0.011	0.002	0.003
rmsd angle (°)	1.45	1.48	1.73	1.71	1.52	1.73	1.65
coordinate error (Å)	0.16	0.07	0.19	0.25	0.21	0.04	0.04
pdb code	2I8O	2I8P	2I8Q	2I8R	2I8S	2I8T	2I8U

[a] The numbers in parentheses correspond to the values for the outermost shell. [b] The ligand is bound to only one copy of the dimer in the asymmetric unit. [c] $R_{merge} = \Sigma|I - \langle I \rangle|/\Sigma I$, where I is the integrated intensity of a given reflection. [d] $R_{crystal} = \Sigma||F_{obs}| - |F_{calc}||/\Sigma|F_{obs}|$. R_{free} was calculated using 5−7% of data excluded from refinement.

manual building. Cross-validation, using 7% of the data for the calculation of the free *R*-factor (*22*), was utilized to monitor building bias. The stereochemistry of the model was routinely monitored throughout the course of refinement using PROCHECK (*23*).

Crystals of wild-type Gmm-Mg^{2+}−GDP and Gmm-Ca^{2+}−GDP-α-D-mannose complexes and His-124 → Leu Gmm−GDP-α-D-mannose, His-124 → Leu Gmm−GDP-α-D-glucose, and His-124 → Leu Gmm−GDP-β-L-fucose complexes were manipulated in a similar fashion. Data from crystals of the wild-type Gmm−GDP complex were collected at COM-CAT (Sector 32ID, Advanced Photon Source, Argonne, IL) using a Mar 165 CCD detector; data from crystals of the His-124 → Leu Gmm−GDP-α-D-mannose and His-124 → Leu Gmm−GDP-α-D-glucose complexes were collected at SER-CAT (Sector 22ID, Advanced Photon Source, Argonne, IL) utilizing a Mar 300 CCD detector; and data for His-124 → Leu Gmm−GDP-β-L-fucose were collected at IMCA-CAT (Sector 17ID, Advanced Photon Source, Argonne, IL) utilizing a ADSC Q4 CCD detector. Data from crystals of the Gmm-Ca^{2+}−GDP-α-D-mannose ternary complex were collected from crystals that were harvested and cryo-preserved immediately after growth (approximately 12 h following the initiation of crystallization) at SER-CAT (Sector 22ID, Advanced Photon Source, Argonne, IL) utilizing a Mar 300 CCD detector. Data from similar crystals of the Gmm-Ca^{2+}−GDP-α-D-mannose ternary complex, which had been allowed to further equilibrate in the crystallization drop for an additional 72 h, were collected at SER-CAT (Sector 22BM, Advanced Photon Source, Argonne, IL) using a Mar 225 CCD detector. Data were collected from two independent crystals for each of the Gmm-Ca^{2+}−GDP-α-D-mannose ternary complexes described above, and the identity of the bound ligand was confirmed in each of the two data sets by analysis of difference Fourier electron density maps. For both Gmm-Ca^{2+}−GDP-α-D-mannose ternary complexes, only the higher resolution data sets were subject to crystallographic refinement including treatment of anisotropic *B*-factors (Table 2).

Because of significant variations in the unit cell parameters among the various ligand cocrystals, the ligand cocrystal structures could not be solved by standard difference Fourier techniques, and several of these structures were outside the radius of convergence of rigid body refinement methods. Therefore, phases for each of these structures were determined by molecular replacement with the program MOLREP (*24*) using the unliganded Gmm structure as a search model. Multiple rounds of manual model building were interspersed with refinement using REFMAC5 (*21*) to complete structure refinement. For the substrate complexes of His-124 → Leu Gmm, density corresponding to the bound ligand was observed in only one copy of the asymmetric unit dimer. Cross-validation used 5−7% of the data in the calculation of the free *R*-factor. The stereochemistry of the model was routinely monitored throughout the course of refinement using PROCHECK (*23*). The refined coordinates have been deposited in the PDB with identification numbers 2I8O (wild-type apo-Gmm), 2I8P (wild-type Gmm−GDP complex),

2I8Q (Gmm His-124 → Leu Gmm−GDP-α-D-mannose complex), 2I8R (Gmm His-124 → Leu Gmm−GDP-α-D-glucose complex), 2I8S (Gmm His-124 → Leu Gmm−GDP-*β*-L-fucose complex), 2I8T (Gmm-Ca^{2+}−GDP-α-D-mannose unreacted ternary complex), and 2I8U (Gmm-Ca^{2+}−GDP reacted product complex).

RESULTS

Kinetic Properties of E. coli O128 Gmm. Kinetic parameters for the hydrolysis of GDP-α-D-mannose by Gmm in the presence of saturating concentrations of magnesium ions were determined. The K_M and k_{cat} for the hydrolytic reaction catalyzed by *E. coli* O128 Gmm are comparable for previously determined values for the enzyme from strain K12 (*10*, *25*). This is to be expected, given the high sequence identity between the two enzymes (over 90%) and the fact that all of the residues within the active site are conserved and may be superimposed (see below). The enzyme requires a divalent metal ion, such as magnesium, for catalysis. Because prior studies with the K12 enzyme demonstrate that manganese may be substituted for magnesium (*11*), we reasoned that substitution of other divalent metals may support catalysis but would compromise efficiency. Kinetic analysis of the hydrolytic reaction with calcium as a divalent metal ion demonstrates a close to 10-fold decrease in catalytic efficiency (k_{cat}/K_M) relative to that of the magnesium-substituted enzyme (see Table 1 for details). As a result of the compromise in catalytic efficiency, substitution of calcium as the divalent metal ion during the crystallization of the Gmm−GDP-α-D-mannose complex yielded crystals of an unreacted ternary complex. Prolonged incubation of these crystals produced a structure of the product complex, demonstrating that the enzyme is active in the crystal.

Overview of the Crystal Structures. In order to determine the structural details of substrate and product recognition along the reaction coordinate of GDP−α-D-mannose hydrolysis, we have determined seven different crystal structures of *E. coli* O128 Gmm: the crystal structure of unliganded enzyme, its binary complex with product GDP, and the binary complex of the inactive site-specific mutant His-124 → Leu Gmm bound to substrates GDP-α-D-mannose, GDP-α-D-glucose, or GDP-*β*-L-fucose, each to resolutions between 1.5 and 2.1 Å. In addition, we also present the crystal structures of the unreacted ternary complex of wild-type Gmm-Ca^{2+}−GDP-α-D-mannose (1.3 Å resolution), from crystals harvested immediately after growth, and of the Gmm-Ca^{2+}−GDP complex (1.4 Å resolution), from equivalent crystals that had been incubated in the crystallization media for an additional 72 h. Each of these structures has been well refined as judged by the following criteria: (1) the residual *R* (and corresponding free *R*) values are within the appropriate range for acceptability for the given resolution of the data, (2) the majority of residues in each of the models fall within the most favored region (90% or greater) or additionally allowed regions of the Ramachandran plot, (3) no additional features are present in difference Fourier maps calculated with phases from the final refined structure, and (4) the stereochemistry of each structure is excellent as judge by the root-mean-square deviations from ideal values (see Table 2 for details).

The overall fold of Gmm is similar in each of the seven crystal structures and is composed of a 20-residue amino terminal helix and loop followed by a 147 residue Nudix domain (*11*, *12*). The structural elements common to the Nudix domain are entirely conserved, and an amino terminal extension first observed in the K12 enzyme structure (*12*) is also present. The structure of wild-type *E. coli* O128 Gmm is essentially identical to that of the K12 enzyme (*12*), as expected from the overall sequence identity of 90% between the two polypeptides. Superposition of the α-carbons of both structures yields a root-mean-square deviation (rmsd) of 0.3 Å for 150 residues. Notably, the active site features, including all catalytically relevant residues, are conserved between the two enzymes. Given the high conservation of structural features and our demonstration of comparable kinetic parameters for the two enzymes, it is likely that the existent biochemical data established for the K-12 enzyme are equally apt for the studies presented here with *E. coli* O128 Gmm (*10*, *25*).

Analytical and preparation gel-filtration chromatographic studies document that *E. coli* O128 Gmm is dimeric in solution, and each of the unliganded and ligand cocrystals of Gmm contains a dimer in the crystallographic asymmetric unit. Dimerization is mediated by an extensive set of polar and nonpolar contacts between the two protomers, with approximately 2510 $Å^2$ surface area buried upon dimerization (as calculated with a probe radius of 1.4 Å). The buried area accounts for about 28% of the total surface area of each individual protomer (accessible surface areas of protomer A = 8891 $Å^2$, protomer B = 8718 $Å^2$). Because the buried surface area exceeds values typical for crystal-packing artifacts (typically 700 $Å^2$) (*26*), the dimer observed in the crystallographic asymmetric unit likely represents the biologically relevant species.

The presence of noncrystallographic symmetry allows two independent views of the protein, ruling out crystallographic packing artifacts in our data analysis. The root-mean-square deviation of the α-carbon positions between the two molecules in each of the crystallographic asymmetric units varies from 0.3 to 1.2 Å. The largest differences between the two molecules in the asymmetric unit are observed in the cocrystal structures of His-124 → Leu Gmm and correspond to changes in the loop region encompassing residues Pro-120 through Asp-126 (see below in Substrate-Induced Conformational Change). Because only one molecule of the dimer contains a bound ligand, the position of this mobile loop varies the greatest between two copies in each of the His-124 → Leu Gmm structures.

Interactions with Substrate and Product

A network of hydrogen bonds mediates the specific recognition of substrates GDP-α-D-mannose, GDP-α-D-glucose, and GDP-*β*-L-fucose and product GDP by Gmm. Unambiguous electron density, corresponding to the position of the respective ligands, can be observed in difference Fourier maps of each cocrystal structure (Figure 2A−D). For the substrate complexes of His-124 → Leu Gmm, density corresponding to the bound ligand was observed in only one copy of the asymmetric unit dimer, presumably because of lattice-packing constraints.

Gmm-Mg^{2+}−GDP Product Complex. In the 1.5 Å resolution cocrystal structure of *E. coli* O128 Gmm bound to product GDP, the guanine nucleotide contributes to the

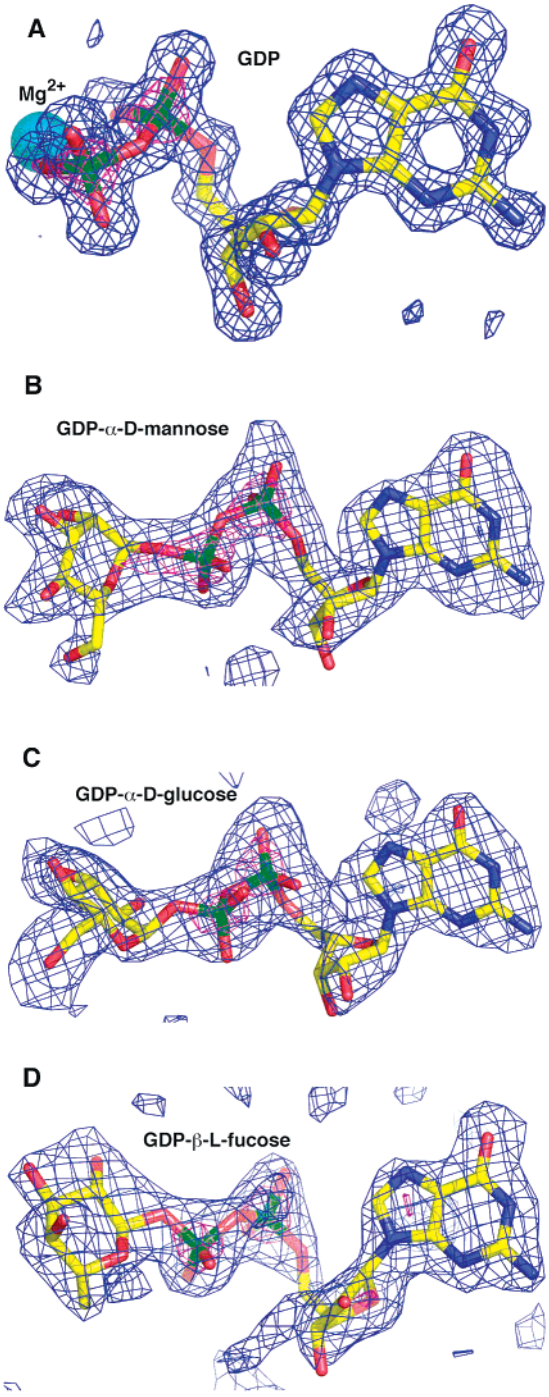

FIGURE 2: Difference Fourier electron density maps, calculated with experimentally determined amplitudes and phases calculated from the final refined structures, minus the appropriate ligand, which have been subject to maximum likelihood refinement with REFMAC5. The coordinates of the final refined structure are superimposed upon the electron density maps. The difference maps correspond to (A) the 1.5 Å resolution cocrystal structure of wild-type Gmm bound to GDP, (B) the 2.0 Å resolution crystal structure of His-124 → Leu Gmm bound to GDP-α-D-mannose, (C) the 2.1 Å resolution crystal structure of Gmm bound to GDP-α-D-glucose, and (D) the 2.0 Å resolution crystal structure of Gmm bound to GDP-β-L-fucose. The contour levels are 2.5 σ (blue) and 8.0 σ (magenta). The catalytically requisite divalent metal (magnesium) is shown as a cyan sphere.

specificity of the recognition of GDP−sugar derivatives from other nucleotide−diphosphate sugars. Several key amino acid residues are involved in hydrogen bonds with the nucleotide, including Arg-52 NH_2−O6 (2.6 Å), Arg-52 Nϵ−N7 (3.0 Å),

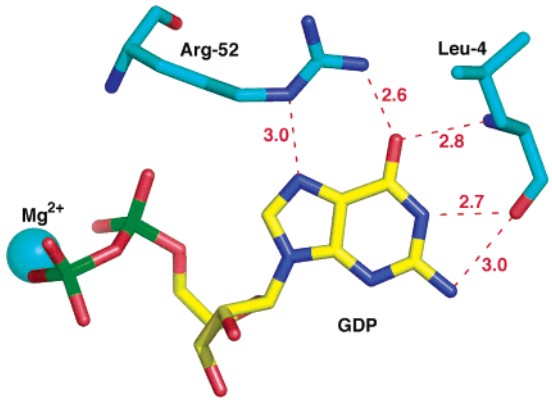

FIGURE 3: Interaction of wild-type Gmm with the guanine nucleotide of product GDP. For clarity, only the hydrogen-bond interactions between the nucleotide and the protein are labeled. The ligand is shown in yellow, and the protein residues are shown in cyan. The catalytically requisite divalent metal (magnesium) is shown as a cyan sphere.

Leu-4 backbone carbonyl-N2 (3.0 Å), Leu-4 backbone carbonyl-N1 (2.7 Å), and Leu-4 backbone amide-O6 (2.8 Å) (Figure 3). The position and orientation of the GDP moiety is slightly altered in each of the substrate complexes, perhaps because of the interactions between the protein and the sugar tail of the substrate. However, each of the component hydrogen bonds involved in the interaction with the nucleotide is still maintained.

His-124 → Leu Gmm−GDP-α-D-mannose Complex. In the 2.0 Å resolution crystal structure of Gmm bound to GDP-α-D-mannose, the sugar moiety of the substrate forms five hydrogen bonds with vicinal enzyme residues, and these hydrogen bonds account for substrate specificity. The 2-hydroxyl of mannose forms hydrogen bonds with Asp-22 Oδ2 (2.7 Å), the 3-hydroxyl hydrogen bonds to Ser-20 Oγ (2.7 Å) and Asp-22 Oδ2 (2.6 Å), and the 4-hydroxyl hydrogen bonds to His-88 Nδ1 (2.7 Å) and Tyr-90 Oη (2.7 Å) (Figure 4A). The branched 6-hydroxyl of mannose is located adjacent to Tyr-90 (Oη−OH distance of 2.7 Å) and engages in a weakly polar interaction with the aromatic ring of Phe-47 (*27*). The guanidinium side chain of Arg-37 further stabilizes the interactions with the ligand by hydrogen bonding to an oxygen atom on the β-phosphate of the nucleotide diphosphate (NH1−O2B distance of 2.9 Å and NH2−O2B distance of 2.9 Å). These interactions result in the tight packing of the α-D-mannose moiety in the active site pocket.

His-124 → Leu Gmm−GDP-α-D-glucose Complex. In the 2.1 Å resolution crystal structure of the binary complex of Gmm with substrate GDP-α-D-glucose, a similar network of hydrogen bonds is also observed. However, α-D-glucose cannot be accommodated in the active site in the same orientation as that of D-mannose because of steric constraints imposed by the change in the position of the 2-hydroxyl from axial to equatorial in glucose. In order to accommodate the pyranose group of glucose and maintain all possible hydrogen-bond interactions, the sugar undergoes a rotation of roughly 25° about the P2−O1B−C1 bond (Figure 4B). This rotation results in a reorientation of the hydrogen-bond donors and acceptors such that the 3-hydroxyl now forms a hydrogen bond with Asp-22 Oδ2 (2.6 Å), and the 4-hydroxyl hydrogen bonds to the Oγ of Ser-20 (2.7 Å) and with Asp-22 (Oδ2−OH distance of 2.8 Å), and the branched 6-hydroxyl forms a hydrogen bond with Tyr-90 (Oη−OH distance of 2.6 Å)

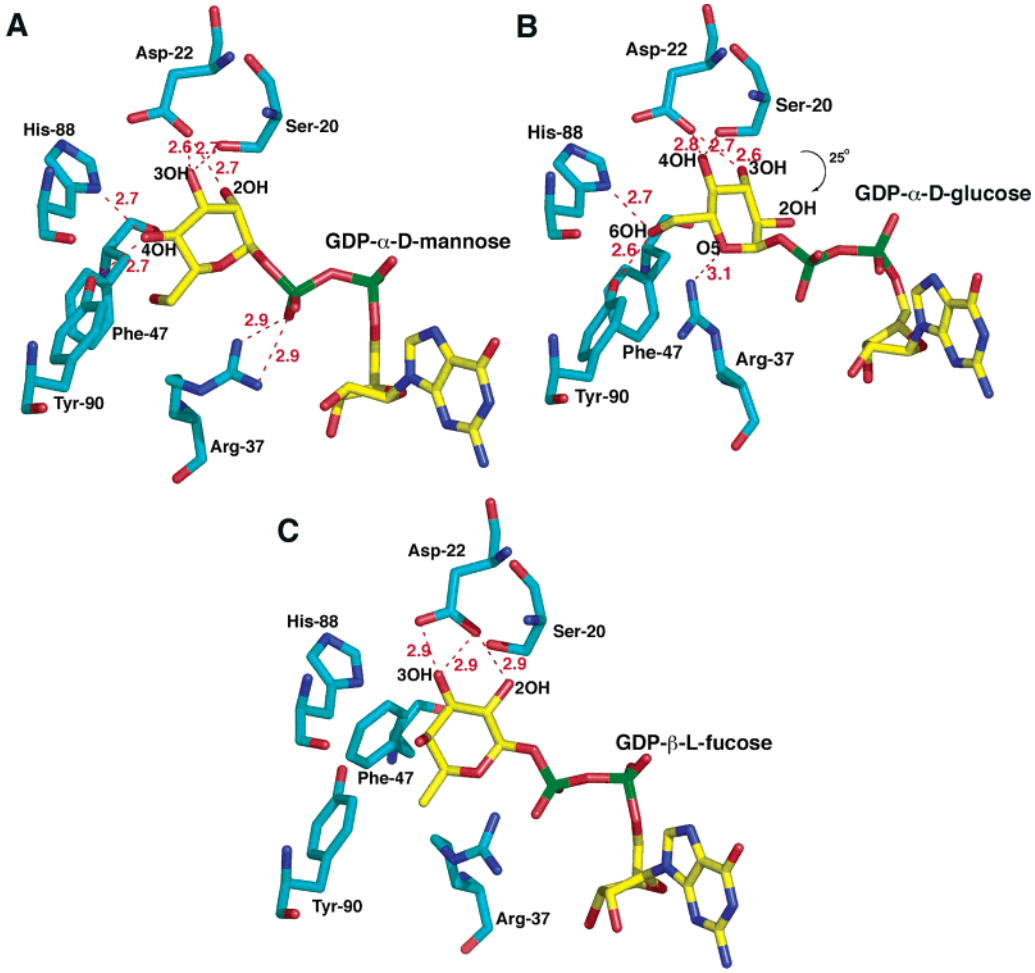

FIGURE 4: Interaction of His-124 → Leu Gmm with sugar nucleotide−diphosphate sugar substrates. For clarity, only the hydrogen-bond interactions between the sugar moiety and the protein are labeled. (A) Interaction with GDP-α-D-mannose: There are five hydrogen bond interactions between the sugar of GDP-α-D-mannose (shown in yellow) and the residues in the active site of Gmm (shown in cyan). Two additional hydrogen bonds are formed between the side chain of Arg-37 and a phosphate oxygen. (B) Interaction with GDP-α-D-glucose: The sugar is rotated approximately 25° relative to that in the Gmm−GDP-α-D-mannose complex. Although the orientation of the sugar has been altered, five hydrogen-bond interactions are still maintained, and the side chain of Arg-37 moves to fill the cavity created by the reorientation of the α-D-glucose sugar. (C) Interaction with GDP-*β*-L-fucose: Only three hydrogen-bond interactions are observed between the *β*-L-fucose sugar and the residues in the active site. Because *β*-L-fucose does not contain a C5-CH_2OH extension, the aromatic side chain of Phe-47 moves closer to form a smaller pocket, which results in increased van der Waals interactions with the sugar.

and His-88 (Nδ1−OH distance of 2.7 Å). Despite this reorientation of hydrogen-bonding partners, the net result is that the number of hydrogen-bond interactions with the sugar moiety is the same as that observed in the cocrystal structure with GDP-α-D-mannose. However, this reorientation results in a cavity between the α-D-glucose group and Phe-47 that is accommodated by movement of the guanidinium side chain of Arg-37 into this cavity, where it can now interact with the O5 of the pyranose (NH_2−O distance of 3.1 Å) (Figure 4B). This movement of Arg-37 results in a loss of the two hydrogen bonds with an oxygen atom on the *β*-phosphate observed in the cocrystal structure with GDP-α-D-mannose (compare Figure 4A and B).

His-124 → Leu Gmm−GDP-β-L-fucose Complex. In the 2.0 Å resolution crystal structure of the binary complex of Gmm with GDP-*β*-L-fucose, there are fewer hydrogen-bond interactions between the protein and the sugar group of the ligand relative to those of the the cocrystal structures with GDP-α-D-mannose and GDP-α-D-glucose. The only hydrogen-bond interactions are between the 3-hydroxyl and Asp-22 Oδ2 (2.9 Å) and Asp-22 Oδ1 (2.9 Å), and the 2-hydroxyl and Asp-22 Oδ2 (2.9 Å) (Figure 4C). The configuration of *β*-L-fucose does not support interactions with either His-88 or Tyr-90. However, replacement of the extended C5-CH_2-OH chain by a C5-CH_3 in fucose results in a small cavity that is accommodated by movement of the aromatic side chain of Phe-47 (compare Figure 4A and C). This movement results in additional van der Waals interactions between the protein and *β*-L-fucose and a tighter packing of the sugar relative to that observed in the cocrystal structure with GDP-α-D-mannose.

Gmm-Ca^{2+}−GDP-α-D-mannose Unreacted Ternary Complex. Kinetic analysis demonstrates that replacement of the catalytically requisite magnesium with calcium results in a close to 10-fold decrease in the catalytic efficiency of Gmm. Data collected from the crystals of the Gmm-Ca^{2+}−GDP-α-D-mannose complex, harvested immediately after crystal growth (approximately 12 h) and continuous electron density corresponding to the substrate GDP-α-D-mannose (Figure 5A) are shown in Figure 5. In the 1.3 Å resolution crystal structure of the wild-type Gmm-Ca^{2+}−GDP-α-D-mannose complex, the position of the sugar moiety and all interacting residues are identical to those observed in the cocrystal

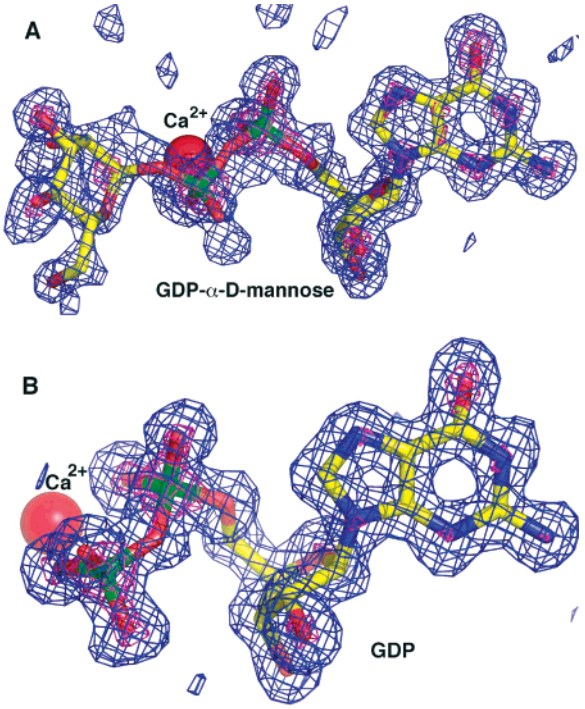

FIGURE 5: Difference Fourier electron density maps, calculated with experimentally determined amplitudes and phases calculated from the final refined structures, minus the appropriate ligand, which have been subject to maximum likelihood refinement with REFMAC5. The coordinates of the final refined structure are superimposed upon the electron density maps. The difference maps correspond to (A) the 1.3 Å resolution cocrystal structure of the wild-type Gmm-Ca^{2+}−GDP-α-D-mannose complex, solved from data collected on the crystals of the ternary complex harvested immediately after growth and (B) the 1.4 Å resolution crystal structure of the wild-type Gmm-Ca^{2+}−GDP product complex, solved from data collected on the crystals of the ternary substrate complex harvested 72 h after crystal growth. The catalytically requisite divalent metal (calcium) is shown as a red sphere. The contour levels are 2.5 σ (blue) and 10 σ (magenta).

structure of His-124 → Leu Gmm bound to GDP-α-D-mannose.

Gmm-Ca^{2+}−GDP Product Ternary Complex. Data collected from crystals of the Gmm-Ca^{2+}−GDP-α-D-mannose complex that had incubated in the crystallization buffer for approximately 72 h at 8 °C reveal an electron density consistent with a product complex (Figure 5B). The 1.4 Å resolution crystal structure of the wild-type Gmm-Ca^{2+}−GDP complex is identical to that of the product Gmm-Mg^{2+}−GDP complex. The position and orientation of the GDP moiety are identical, and each of the hydrogen bonds involved in the interaction with the nucleotide is maintained.

Substrate-Induced Conformational Change. Progress along the reaction coordinate of the hydrolytic reaction is accompanied by significant rearrangement of atoms in the enzyme active site. In the absence of the substrate or product, a loop encompassing residues Pro-120−Asp-126 is positioned away from the enzyme core, toward the bulk solvent (Figure 6). This loop contains the putative catalytic base His-124, and the displacement of this region away from the enzyme core results in an ill-formed active site (the open orientation). The open orientation of the active site region is observed in each of the two copies of Gmm observed in the crystallographic asymmetric unit, albeit with slightly different dispositions.

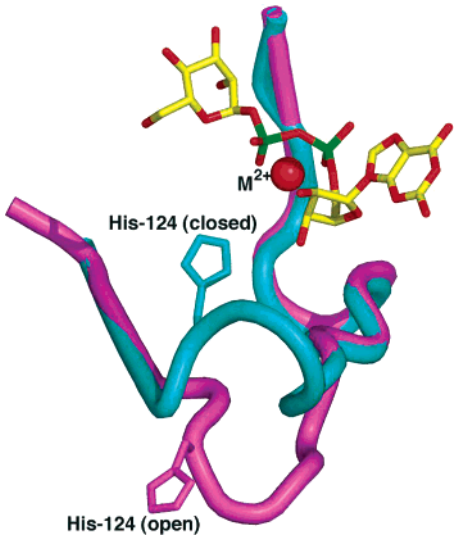

FIGURE 6: Superposition of the ribbons diagrams of the active site loop observed in the crystal structures of apo-Gmm and the Gmm-Ca^{2+}−GDP-α-D-mannose substrate complex. The purple ribbon diagram shows the backbone trace of apo-Gmm around residues 110−130, with the active site His-124 shown as a stick figure. Note that in the absence of the ligand, a loop harboring catalytically important residues is positioned away from the enzyme core toward the bulk solvent. The cyan ribbon diagram shows a trace of the equivalent residues observed in the Gmm-Ca^{2+}−GDP-α-D-mannose substrate complex. A catalytically competent active site is formed in the presence of the appropriate substrate. The substrate GDP-α-D-mannose is shown as a yellow stick figure, and the requisite metal ion is shown as a red sphere.

In molecule A, the residues encompassing this loop region are displaced an average of 5 Å relative to their respective positions in molecule B. The rms deviation between the loop residues of the two molecules is as follows: Pro-120 (5.8 Å), Asp-121 (5.5 Å), Glu-122 (5.7 Å), Gln-123 (5.5 Å), His-124 (5.3 Å), Asp-125 (2.5 Å), and Asp-126 (4.3 Å). In the open orientation, a total of 15 water molecules occupy the shallow region of the active site.

Upon binding to the substrate (GDP-α-D-mannose and Ca^{2+}) or product (GDP and Mg^{2+}), this loop region undergoes a significant reorientation toward the core of the enzyme (the closed orientation) (Figure 6). In comparison with the structure of the unliganded enzyme, the average displacement of the residues within this loop is as follows: Pro-120 (5.4 Å), Asp-121 (6.2 Å), Glu-122 (7.7 Å), Gln-123 (8.3 Å), His-124 (6.2 Å), Asp-125 (3.9 Å), and Asp-126 (2.2 Å) (total rmsd = 4.4 Å for all atoms in this loop). This movement results in the formation of a well-defined internal cavity that houses the products and presumably the substrate. A network of hydrogen bonds stabilizes the closed orientation of this loop and positions the putative catalytic base His-124 for catalysis. In addition, the divalent metal ion interacts with the carbonyl of Gln-123 (2.1 Å distance) and also participates in stabilizing the hydrogen-bonding network of water molecules in the active site. The position of each residue within this loop in the Gmm-Ca^{2+}−GDP-α-D-mannose and Gmm- Mg^{2+}−GDP structures is nearly identical between the two molecules within the crystallographic asymmetric unit (rmsd of 0.2 Å). Stable interactions between the catalytically requisite divalent calcium or magnesium ion, the GDP substrate, or the GDP-α-D-mannose product and a host of associated water molecules facilitate the formation of a compact structure with appropriate active site residues poised

for catalysis. Finally, we note that the residues within this loop are ill defined in our structures of the His-124 → Leu Gmm substrate complex, presumably as a consequence of the fact that the mutant Leu-124 side chain is not capable of forming the requisite hydrogen bonds necessary for the formation of a stable active site cavity.

DISCUSSION

We present here seven crystal structures of the Nudix hydrolase Gmm in apo form and in complex with various substrates and products. Cocrystal structures of Gmm bound to GDP-α-D-mannose, GDP-α-D-glucose, and GDP-β-L-fucose were of a catalytically inactive site-specific variant in which the active site His-124 has been replaced with a Leu. Because residues in the loop region encompassing this residue are ill-defined in each of these crystal structures, it is important to establish that the binding mode of these substrates observed in the cocrystal structures of His-124 → Leu Gmm reflect productive complexes and that each of these observed species lies along the reaction coordinate. In order to do this, we sought to identify a substituted divalent metal ion for the catalytically requisite magnesium, which would compromise catalytic efficiency but still support turnover with the aim of trapping a pre-catalytic ternary complex for crystallographic analysis. Our kinetic studies establish that replacement with calcium results in a close to 10-fold decrease in k_{cat}/K_M for the enzyme with GDP-α-D-mannose as a substrate.

Substrate Turnover in Crystals of Ca^{2+}-Gmm. The structure of the Gmm-Ca^{2+}−GDP-α-D-mannose complex, determined from the crystals of the ternary complex harvested immediately after crystal growth, reveals an unreacted ternary complex (Figure 5A). Comparison of the crystal structures of the Gmm-Ca^{2+}−GDP-α-D-mannose complex with that of the His-124 → Leu Gmm−GDP-α-D-mannose complex confirms that the His-124 → Leu mutation does not affect the binding or orientation of the sugar. We also determined the structure of the ternary complex from crystals that had been incubated in the crystallization drop for an additional 72 h, and this structure reveals a Gmm-Ca^{2+}−GDP complex (Figure 5B), demonstrating that the enzyme is active in the crystal and that the unreacted ternary complex likely represents the Michaelis complex. The orientation of the substrate in the unreacted Gmm-Ca^{2+}−GDP-α-D-mannose ternary complex is identical to that observed in the His-124 → Leu Gmm−GDP-α-D-mannose complex. Thus, the His-124 → Leu mutation does not affect the binding mode of the substrate relative to that observed in the wild-type Gmm-Ca^{2+} complex, and the binding mode of the substrates observed in each of the cocrystal structures of His-124 → Leu Gmm likely represents a productive complex along the reaction coordinate.

Molecular Basis for Substrate and Product Recognition. Prior biochemical studies have established kinetic parameters for the hydrolysis of various substrates by Gmm (*10*, *25*). Although these studies utilized the enzyme from *E. coli* strain K12, the results can be applied to the *E. coli* O128 enzyme under study here, given the high overall sequence identity between the two proteins (approximately 90%), the structural and sequence conservation of residues in the active site, and our demonstration that the kinetic parameters for hydrolysis of the substrate GDP-α-D-mannose by *E. coli* O128 Gmm are comparable to those reported for the enzyme from *E. coli* strain K12 (*10*, *25*). Although Gmm can hydrolyze both GDP-α-D-glucose and GDP-α-D-mannose, with GDP-α-D-glucose as a substrate, the K_M is higher relative to that for GDP-α-D-mannose (2.9-fold and 4.3-fold, respectively) (*25*). Hence, the affinity for the substrate GDP-α-D-glucose is lower. Additionally, although GDP-β-L-fucose is a poor substrate for Gmm (k_{cat} is 58-fold lower), the affinity of the enzyme for this nucleotide−diphosphate sugar is higher than that for GDP-α-D-mannose (K_M is 6-fold lower) (*25*). Our structural results may help reconcile these observed difference in substrate binding.

On the basis of the comparisons of our cocrystal structures of the His-124 → Leu Gmm−GDP-α-D-mannose and Gmm−GDP-α-D-glucose complexes, we can postulate the basis for the decreased affinity for GDP-α-D-glucose. In our cocrystal structures, α-D-glucose cannot be accommodated in the active site in the same position as that of α-D-mannose because of steric constraints and undergoes a rotation of roughly 25° about the P2−O1B−C1 bond (compare Figure 4A and B). Although the net result of this reorientation maintains the same number of hydrogen bonds to the sugar moiety as that observed in the GDP-α-D-mannose cocrystal structure, this movement creates a cavity between the sugar and Phe-47. The side chain of Arg-37 moves to fill up a cavity adjacent to the α-D-glucose, resulting in the loss of two hydrogen bonds with an oxygen atom on the β-phosphate. Consequently, the imperfect packing of the α-D-glucose sugar and the loss of these two hydrogen bonds likely result in the decreased affinity of Gmm for GDP-α-D-glucose relative to that for GDP-α-D-mannose.

Our cocrystal structures may also explain the previously observed increase in affinity of Gmm for GDP-β-L-fucose as a substrate (*25*). Replacement of the extended C5-CH_2-OH chain by a C5-CH_3 in β-L-fucose results in a small cavity that is accommodated by the movement of the side chain of Phe-47 (compare Figure 4A and C). This rearrangement results in the tighter packing of the sugar in the active site pocket relative to that observed in the structure of GDP-α-D-mannose, accounting for the reported decrease in K_M with GDP-β-L-fucose as the substrate (*25*).

Concerted Conformational Changes along the Reaction Coordinate. A comparison of the structure of unliganded Gmm with that of the Gmm-Ca^{2+}−GDP-α-D-mannose substrate and Gmm-Mg^{2+}−GDP product complex reveals a significant movement of the loop-encompassing residues Pro-120−Asp-126, containing the putative catalytic base His-124 (Figure 6). In the crystal structures of the related Nudix enzymes *E. coli* ADP-ribose pyrophosphatase (*28*, *29*) and *M. tuberculosis* ADP-ribose pyrophosphatase (*30*), the respective catalytic bases are disordered in the absence of the substrate and become anchored upon the binding of three metal ions and the substrate. Similarly, our structures illustrate the first example of the substrate-induced formation of a catalytically competent active site for the glycosyl hydrolase class of Nudix enzymes. The concerted changes observed in our crystal structures illustrate gross movements toward the formation of a functional active site architecture that accompanies progress along the reaction coordinate (Figure 6).

The ordered structural transition observed in the case of the pyrophosphatases has been interpreted as a mechanism to ensure substrate specificity against ubiquitous high-energy phosphates (*28*). It is likely that the concerted movement of the catalytic base containing loop residues of Gmm serves an analogous role in catalytic specificity. Given the prevalence of sugar polymers encoded within the LPS component of the bacterial outer membrane, residual hydrolytic activity against mannose (or glucose) linked sugars would be detrimental to the viability of the organism. The substrate/product induced conformational changes in this loop region, to form a catalytically competent active site architecture, would ensure specificity toward glucose or mannose nucleotide−diphosphate sugars over other important sugar conjugates.

Given the role of LPS in the persistence of pathogenic bacteria, the enzymes that carry out their biosynthesis are viable targets for therapeutic intervention (*31*, *32*). Our structures provide insights aiding such design efforts. Although GDP-β-L-fucose itself would not be an effective inhibitor because Gmm shows residual activity against this nucleotide−diphosphate sugar (*25*), guanine dinucleotide sugar analogues that mimic the structure of GDP-β-L-fucose and exploit the protein−ligand interactions observed in our cocrystal structure would be viable inhibitors. The disruption of Gmm activity by such inhibitors would result in a decrease in the diversity of the *O*-antigen. *E. coli* strains lacking the *O*-antigen have been shown to be more susceptible to the bactericidal effects of normal human serum (*33*, *34*).

ACKNOWLEDGMENT

We thank Keith Brister (BioCARS, Beamline 14-ID), Lisa Keefe (IMCA-CAT, Beamline 17-ID), and Marie Graham (Southeast Regional Collaborative Access Team, Beamlines 22-ID and 22-BM) for assistance with synchrotron data collection and N.G. Wetters for assistance with crystallization. We also thank W. A. van der Donk and M. V. Lasker for the critical reading of this manuscript.

REFERENCES

1. Yoshida, M., Rietschel, E. T., Galanos, C., Hirata, M., Luderitz, O., and Westphal, O. (1972) Hemorrhage and necrosis in the bone marrow by lipid A, *Jpn. J. Med. Sci. Biol 25*, 238−242.
2. Nowotny, A., Behling, U. H., and Chang, H. L. (1975) Relation of structure to function in bacterial endotoxins. VIII. Biological activities in a polysaccharide-rich fraction, *J. Immunol. 115*, 199−203.
3. Adorini, L., Ruco, L., Uccini, S., De Franceschi, G. S., Baroni, C. D., and Doria, G. (1976) Biological effects of Escherichia coli lipopolysaccharide (LPS) in vivo. II. Selection in the mouse thymus of PHA- and con A-responsive cells, *Immunology 31*, 225−232.
4. Samuel, G., and Reeves, P. (2003) Biosynthesis of O-antigens: genes and pathways involved in nucleotide sugar precursor synthesis and O-antigen assembly, *Carbohydr. Res. 338*, 2503−2519.
5. Raetz, C. R., and Whitfield, C. (2002) Lipopolysaccharide endotoxins, *Annu. Rev. Biochem. 71*, 635−700.
6. Whitfield, C., Kaniuk, N., and Frirdich, E. (2003) Molecular insights into the assembly and diversity of the outer core oligosaccharide in lipopolysaccharides from *Escherichia coli* and *Salmonella*, *J. Endotoxin Res. 9*, 244−249.
7. Reeves, P. R., Hobbs, M., Valvano, M., Skurnik, M., Whitfield, C., Coplin, D., Kido, N., Klena, J., Maskell, D., Raetz, C., and Rick. P. (1996) Bacterial polysaccharide synthesis and gene nomenclature, *Trends Microbiol. 4*, 495−503.
8. Wang, L., and Reeves, P. R. (2000) The *Escherichia coli* O111 and *Salmonella enterica* O35 gene clusters: gene clusters encoding the same colitose-containing O-antigen are highly conserved, *J. Bacteriol. 182*, 5256−5261.
9. Frick, D. N., Townsend, B. D., and Bessman, M. J. (1995) A novel GDP-mannose mannosyl hydrolase shares homology with the MutT family of enzymes, *J. Biol. Chem. 270*, 24086−24091.
10. Legler, P. M., Massiah, M. A., Bessman, M. J., and Mildvan, A. S. (2000) GDP-mannose mannosyl hydrolase catalyzes nucleophilic substitution at carbon, unlike all other Nudix hydrolases, *Biochemistry 39*, 8603−8608.
11. Mildvan, A. S., Xia, Z., Azurmendi, H. F., Saraswat, V., Legler, P. M., Massiah, M. A., Gabelli, S. B., Bianchet, M. A., Kang, L. W., and Amzel, L. M. (2005) Structures and mechanisms of Nudix hydrolases, *Arch. Biochem. Biophys. 433*, 129−143.
12. Gabelli, S. B., Bianchet, M. A., Azurmendi, H. F., Xia, Z., Sarawat, V., Mildvan, A. S., and Amzel, L. M. (2004) Structure and mechanism of GDP-mannose glycosyl hydrolase, a Nudix enzyme that cleaves at carbon instead of phosphorus, *Structure (Cambridge, MA, U.S.) 12*, 927−935.
13. Sengupta, P., Bhattacharyya, T., Shashkov, A. S., Kochanowski, H., and Basu, S. (1995) Structure of the O-specific side chain of the Escherichia coli O128 lipopolysaccharide, *Carbohydr. Res. 22*, 283−290.
14. Sambrook, J., Fritsch, E. F., and Maniatis, T. (1989) *Molecular Cloning: A Laboratory Manual*, 2nd ed. Cold Spring Harbor Laboratory Press, New York.
15. Shao, J., Li, M., Jia, Q., Lu, Y., and Wang, P. G. (2003) Sequence of *Escherichia coli* O128 antigen biosynthesis cluster and functional identification of an alpha-1,2-fucosyltransferase, *FEBS Lett. 553*, 99−103.
16. Van Duyne, G. D., Standaert, R. F., Karplus, P. A., Schreiber, S. L., and Clardy, J. (1993) Atomic structures of the human immunophilin FKBP-12 complexes with FK506 and rapamycin, *J. Mol. Biol. 229*, 105−124.
17. Otwinowski, Z., and Minor, W. (1997) Processing of X-ray diffraction data collected in oscillation mode, *Methods Enzymol. 276*, 307−326.
18. Terwilliger, T. C. (2003) SOLVE and RESOLVE: automated structure solution and density modification, *Methods Enzymol. 374*, 22−37.
19. Terwilliger, T. C. (2002) Automated side-chain model-building and sequence assignment by template-matching, *Acta Crystallogr., Sect. D 59*, 45−49.
20. McRee, D. E. (1999) XtalView/Xfit−A versatile program for manipulating atomic coordinates and electron density, *J. Struct. Biol. 125*, 156−165.
21. Murshudov, G. N., Vagin, A. A., and Dodson, E. J. (1997) Refinement of macromolecular structures by the maximum-likelihood method, *Acta Crystallogr., Sect. D 53*, 240−255.
22. Brünger, A. T. (1993) Assessment of phase accuracy by cross validation: the free R value. Methods and applications, *Acta Crystallogr., Sect. D 49*, 24−36.
23. Laskowski, R. A. (2003) Structural quality assurance, *Methods Biochem. Anal. 44*, 273−303.
24. Vagin, A., and Teplyakov, A. (2000) An approach to multi-copy search in molecular replacement, *Acta Crystallogr., Sect. D 56* 1622−1624.
25. Xia, Z., Azurmendi, H. F., Lairson, L. L., Withers, S. G., Gabelli, S. B., Bianchet, M. A., Amzel, L. M., and Mildvan, A. S. (2005) Mutational, structural, and kinetic evidence for a dissociative mechanism in the GDP-mannose mannosyl hydrolase reaction, *Biochemistry 28*, 8989−8997.
26. Janin, J. (1997) Specific versus non-specific contacts in protein crystals, *Nat. Struct. Biol. 4*, 973−974.
27. Burley, S. K., and Petsko, G. A. (1988) Weakly polar interactions in proteins, *Adv. Protein Chem. 39*, 125−189.
28. Gabelli, S. B., Bianchet, M. A., Bessman, M. J., and Amzel, L. M. (2001) The structure of ADP-ribose pyrophosphatase reveals the structural basis for the versatility of the Nudix family, *Nat. Struct. Biol. 8*, 467−472.
29. Gabelli, S. B., Bianchet, M. A., Ohnishi, Y., Ichikawa, Y., Bessman, M. J., and Amzel, L. M. (2002) Mechanism of the *Escherichia coli* ADP-ribose pyrophosphatase, a Nudix hydrolase, *Biochemistry 41*, 9279−9285.

30. Kang, L. W., Gabelli, S. B., Cunningham, J. E., O'Handley, S. F., and Amzel, L. M. (2003) Structure and mechanism of MT-ADPRase, a nudix hydrolase from *Mycobacterium tuberculosis*, *Structure (Cambridge, MA, U.S.) 11*, 1015−1023.
31. Heath, R. J., White, S. W., and Rock, C. O. (2001) Lipid biosynthesis as a target for antibacterial agents, *Prog. Lipid Res. 40*, 467−497.
32. Yethon, J. A., and Whitfield, C. (2001) Lipopolysaccharide as a target for the development of novel therapeutics in gram-negative bacteria, *Curr. Drug Targets*: *Infect. Disord. 1*, 91−106.
33. Stawski, G, Nielsen, L, Orskov, F., and Orskov, I. (1990) Serum sensitivity of a diversity of *Escherichia coli* antigenic reference strains. Correlation with an LPS variation phenomenon, *APMIS 98*, 828−838.
34. Burns, S. M., and Hull, S. I. (1998) Comparison of loss of serum resistance by defined lipopolysaccharide mutants and an acapsular mutant of uropathogenic *Escherichia coli* O75:K5, *Infect. Immun. 66*, 4244−4253.

BI061056U